




Growth of magnetic graphene films with higher electromagnetic interference shielding at moderate annealing temperatures

Wei Liu^{1,2,3}, Kun Jia³, Donghong Wang³, Xuehong Wei^{1,*} , Peng Wang³, and Kai Zheng³

¹ College of Chemistry and Chemical Engineering, Shanxi University, Taiyuan 030006, China

² College of Chemistry and Molecular Engineering, Peking University, Beijing 100871, China

³ Shanxi Key Laboratory of Electromagnetic Protection Materials and Technology, 33rd Research Institute of China Electronics Technology Group Corporation, Taiyuan 030006, China

Received: 3 June 2022

Accepted: 13 September 2022

Published online:
22 September 2022

© The Author(s), under exclusive licence to Springer Science+Business Media, LLC, part of Springer Nature 2022

ABSTRACT

Ultrathin, highly conductive, and free-standing graphene films have been seen as promising electromagnetic interference (EMI) shielding materials for portable electronic devices. However, they are still expensive. In this paper, a magnetic graphene film decorated with Fe₃O₄ nanoparticles was prepared through in situ wet chemical synthesis followed by catalytic graphitization. A graphitic structure was obtained at a moderate annealing temperature (1000 °C), after introducing Fe₃O₄ nanoparticles. This temperature is much lower than the conventional graphitization temperature, which reduces the synthesis costs of graphene film. In addition, Fe₃O₄ also behaved as microwave absorbers, enhancing the EMI shielding performances. The resulting ultrathin film (~ 50 μm) provided a high EMI shielding effectiveness (SE) of ~ 52.76 dB in the X-band (8.2–12.4 GHz). This is found to be higher than that of bare graphene films (~ 33.45 dB) prepared under the same temperature and sufficient to screen about 99.999% of microwave radiation. Furthermore, absorption was the dominant shielding mechanism for the prepared film owing to the contribution of Fe₃O₄ nanoparticles that reduced the electromagnetic pollution resulting from secondary reflections. The catalytic graphitization strategy could provide a low-cost approach for fabricating efficient graphene-based EMI shielding materials for portable electronic device applications.

Address correspondence to E-mail: xhwei@sxu.edu.cn; weixh2019@126.com

1 Introduction

The rapid development of information technology and electronic devices has inevitably caused serious pollution through electromagnetic radiation, which not only interferes with the normal operation of electronic components but also threatens the environment and human health [1–4]. Electromagnetic interference (EMI) shielding is one of the most important and effective approaches for reducing the negative impact of stray electromagnetic radiation [5]. Metals and alloys are traditional choices for EMI shielding materials because of their high conductivity; however, they suffer from high density, easy corrosion, and rigidity, which are undesirable in portable and wearable electronic devices [6, 7]. Moreover, metals provide EMI shielding predominantly through reflection, which can cause secondary electromagnetic pollution. Therefore, it is necessary to develop new lightweight and flexible EMI shielding materials to reduce the impact of EMI on portable and wearable electronic devices.

Graphene, a new type of two-dimensional carbon nanomaterial, is becoming a promising candidate for EMI shielding due to its low density, corrosion resistance, high carrier mobility, and modifiable surface properties [8–10]. Several efforts have been made to introduce graphene into polymer matrices. However, poor dispersion of graphene in polymer matrix limits its use as composite filler [11–14]. In addition, the thickness of polymer-based composites is usually more than 1 mm, which is difficult to meet the requirement of EMI materials for portable and wearable devices. Recently, free-standing graphene films derived from graphene oxide (GO) have attracted significant interest from researchers because of their exceptional properties, such as low density, ultrathin thickness, flexibility, good processability, ultrahigh thermal and electrical conductivity [15–18]. There are numerous oxygen-containing functional groups and structural defects on the surface of GO, which makes its conductivity very poor [16, 18]. Most functional groups can be removed by chemical reduction or moderate thermal annealing (< 2000 °C), but such prepared reduced graphene oxide (RGO) films still have a large number of structural defects, which can be repaired through further high-temperature graphitization to highly crystalline graphene film. For example, Shen et al.

[15] fabricated an 8.4- μm -thick graphene film by the direct evaporation of a GO suspension followed by graphitization at 2000 °C; the film exhibited an EMI shielding effectiveness (SE) of 20 dB in the X-band. Lin et al. [19] modified GO with ethylenediamine to obtain amine-modified GO films, which was subsequently graphitized at 2600 °C to prepare a nitrogen-doping graphene film with an EMI SE of 58.5 dB. Furthermore, Wang et al. [20] annealed GO film at an ultrahigh temperature of 3000 °C and deposited a copper layer on graphene film via magnetron sputtering; the EMI SE of this composite film can reach as high as 63 dB. However, ultrahigh-temperature graphitization consumes substantial energy and time, which increases the production cost of the graphene films. Moreover, the achievement of such high annealing temperature also requires special equipment. It is still a big challenge to prepare highly crystalline graphene films at a relatively low temperature (< 2000 °C).

Catalytic graphitization is an effective method to obtain a graphitic structure at a moderate temperature in the presence of various catalysts, such as boron [21], nickel [22, 23], or iron [24, 25]. The graphitization temperature of carbon precursors can be remarkably decreased using this strategy, thereby reducing the production cost of graphitic materials. The catalytic graphitization effect of Fe_3O_4 has been demonstrated by previous works [25–27]. For instance, Zhang et al. [25] discovered the graphitic structure in polyacrylonitrile-based carbon nanofibers carbonized at 800 °C with the aid of Fe_3O_4 . Mordina et al. [26] revealed that Fe_3O_4 increased the graphitization degree and the conductivity of nanofibers at a carbonization temperature of 900 °C. Although there were already some reports on Fe_3O_4 /RGO composite materials [28–30], highly crystalline graphene films have not been obtained due to the absence of graphitization process. To our best knowledge, using catalytic graphitization effect to fabricate highly crystalline graphene films has not been reported so far.

In the present work, we used catalytic graphitization induced by Fe_3O_4 nanoparticles to prepare EMI shielding graphene films at moderate annealing temperatures (1000 °C), wherein Fe_3O_4 nanoparticles were embedded onto graphene films via in situ wet chemical synthesis. Furthermore, we characterized the microstructure, thermal and electrical conductivity and EMI shielding performances of the grown

Fe₃O₄@graphene films (Fe₃O₄@GF) and discussed the catalytic graphitization effect and EMI shielding mechanism. The Fe₃O₄@GF exhibited a high thermal conductivity of 973 W m⁻¹ K⁻¹ and an electrical conductivity of $\sim 2.0 \times 10^3$ S cm⁻¹. Moreover, the EMI SE of Fe₃O₄@GF can reach as high as 52.76 dB in the X-band, and absorption is the dominant shielding mechanism.

2 Experimental procedure and investigation

2.1 Preparation of Fe₃O₄@GO film

The Fe₃O₄@GO film was prepared by in situ wet chemical synthesis followed by vacuum filtration. First, a GO aqueous suspension (~ 2 mg/mL) was obtained by sonicating a mixture of graphite oxide that was prepared by the Hummers method and distilled water at 100 W for 5 min. Subsequently, a 50 mL of aqueous solution containing 2 mmol of FeCl₂ and 4 mmol of FeCl₃ was added into 150 mL of the above GO suspension and stirred for 8 h. Then, 8 mL of ammonia solution with the concentration of 25–28 wt% was added dropwise into the mixture with continuous stirring to synthesize Fe₃O₄. These processes were performed in an argon atmosphere. A black precipitate was obtained by centrifuging the resulting mixture, which was washed several times with distilled water before redispersion. Finally, Fe₃O₄@GO film was prepared by filtering the redispersed suspension through a Teflon film with a pore size of 200 nm, followed by drying and peeling from the substrate.

2.2 Preparation of Fe₃O₄@GF

Fe₃O₄@GO film was placed into a common tubular furnace and annealed at 1000 °C for 2 h under an argon atmosphere with the heating rate of 2 °C/min. The obtained black film was Fe₃O₄@GF. For comparison, the RGO film (RGF) was prepared by annealing bare GO film under the same preparation condition. Moreover, highly crystalline graphene film (HCGF) was prepared at 2800 °C under an argon atmosphere.

2.3 Characterization

The structure and morphology of the Fe₃O₄@GF were observed by a field emission scanning electron microscopy (FE-SEM, JEOL JSM-7001F) and transmission electron microscopy (TEM, FEI Tecnai G2 F30). The crystalline structure of the Fe₃O₄@GF was tested by powder X-ray diffraction (XRD) using a Bruker D8 Advance Diffractometer with Cu K α ($\lambda = 1.54184$ Å) radiation. The X-ray photoelectron spectroscopic (XPS) was performed an X-ray photoelectron spectrometer (Thermo Fisher, ESCALAB 250Xi) equipped with a monochromatic Al K α X-ray source. The Raman spectra were recorded from 500 to 3000 cm⁻¹ on a confocal Raman Microprobe (Labram Aramis) using the 532 nm excitation line of an Argon-ion laser. Thermal degradations were investigated by a thermogravimetric analyzer (TGA, PE STA8000) under an oxygen atmosphere with a heating rate of 10 °C min⁻¹. The electrical conductivity of the samples was measured by a digital four-probe tester (ST-2258A). The thermal conductivity of the samples was calculated by using the equation $\kappa = \alpha \times C_p \times \rho$, where κ , α , C_p , and ρ represent thermal conductivity, thermal diffusivity, heat capacity, and sample density, respectively. The thermal diffusivity and heat capacity were measured using a laser flash method (Netzsch, LFA-447) at room temperature. The EMI SE of samples in the frequency of 8.2–12.4 GHz was tested by a vector network analyzer (Agilent, N5247A) based on waveguide method.

3 Results and discussion

3.1 Growth mechanism of Fe₃O₄ on graphene film

The Fe₃O₄@GF was prepared through in situ growth of Fe₃O₄ nanoparticles on GO film followed by the graphitization of GO. The growth mechanism of Fe₃O₄ nanoparticles and formation of Fe₃O₄@GF are illustrated in Fig. 1. Initially, the GO suspension mingles with the Fe²⁺/Fe³⁺ solution, following which excessive ammonia is added to the resulting solution. Fe₃O₄ nanoparticles are synthesized via the following reaction [28, 29].

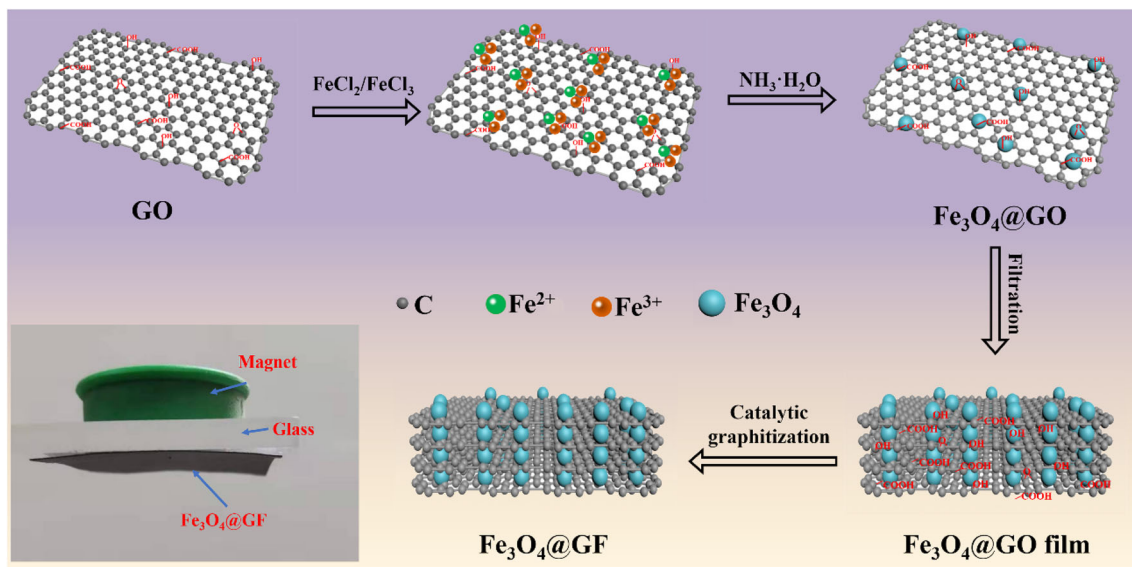
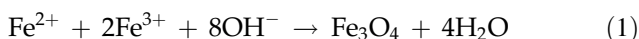


Fig. 1 Schematic representation of the growth mechanism of Fe_3O_4 nanoparticles on graphene film



The presence of oxygen-containing functional groups, such as carboxyl ($-\text{COOH}$), hydroxyl ($\text{C}-\text{OH}$), and epoxy ($\text{C}-\text{O}-\text{C}$) groups, negatively charges the GO surface; hence, it can electrostatically attract cations (Fe^{2+} and Fe^{3+}) in the solution [29, 30]. Subsequently, these oxygen-containing functional groups evolve into active sites for the nucleation and growth of Fe_3O_4 nanoparticles [30]. Finally, with the removal of oxygen-containing functional groups by annealing treatment, we obtained $\text{Fe}_3\text{O}_4@\text{GF}$ that can be strongly attracted by a magnet, showing a ferromagnetic characteristic.

3.2 Morphologies of $\text{Fe}_3\text{O}_4@\text{GF}$

To investigate the distribution of Fe_3O_4 nanoparticles on the graphene surface, the morphological features of RGF, HCGF, and $\text{Fe}_3\text{O}_4@\text{GF}$ were observed by SEM. Compared with the rough surface and loose structure of RGF (Fig. 2a, d), HCGF exhibits a smooth surface and well-stacked multilayer structure (Fig. 2b, e), which can be attributed to the repair of structural defects on graphene film during high-temperature graphitization. In the case of $\text{Fe}_3\text{O}_4@\text{GF}$, plenty of spherical nanoparticles are uniformly anchored on the surface of the graphene film (Fig. 2c) and intercalated between graphene layers (Fig. 2f). These spherical particles are identified as Fe_3O_4 by energy-dispersive spectrum (Fig. S1). The

intercalation of Fe_3O_4 nanoparticles hardly affects the well-stacked multilayered structure of the graphene film.

The morphologies of $\text{Fe}_3\text{O}_4@\text{GF}$ were further observed by TEM. TEM images of $\text{Fe}_3\text{O}_4@\text{GF}$ also reveal that the graphene sheet is homogeneously decorated by numerous Fe_3O_4 nanoparticles with diameters ranging from 5 to 15 nm (Fig. 3a). Note that Fe_3O_4 nanoparticles remain firmly attached to the surface of the graphene sheets even after severe ultrasonic oscillation during TEM sample preparation, indicating strong interfacial bonding between graphene nanosheets and Fe_3O_4 nanoparticles. Furthermore, high-resolution TEM images of Fe_3O_4 crystalline grains reveal a lattice spacing of ~ 0.25 nm (Fig. 3b), corresponding to the (311) plane of Fe_3O_4 [31].

3.3 Structural evolution of $\text{Fe}_3\text{O}_4@\text{GF}$

To explore the catalytic graphitization mechanism of Fe_3O_4 nanoparticles, the phase compositions of samples were tested by XRD. Figure 4 shows the XRD patterns of samples. For $\text{Fe}_3\text{O}_4@\text{GO}$ film, a strong diffraction peak can be observed at $2\theta = 11.8^\circ$, which can be ascribed to GO. In addition, several weak diffraction peaks appear at $2\theta = 30.2^\circ, 35.6^\circ, 43.2^\circ, 53.6^\circ, 57.2^\circ,$ and 62.8° , corresponding to the (220), (311), (400), (422), (511), and (440) planes of face-centered cubic Fe_3O_4 [28–31]. After thermal annealing, the strong diffraction peak shifts from 11.8 to

Fig. 2 Top-view SEM images of **a** RGF, **b** HCGF, and **c** Fe₃O₄@GF. Cross-section SEM images of **d** RGF, **e** HCGF, and **f** Fe₃O₄@GF

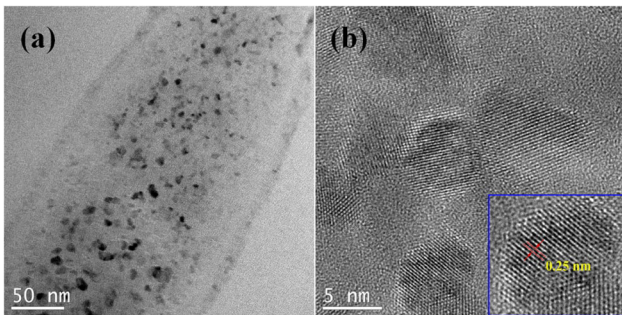
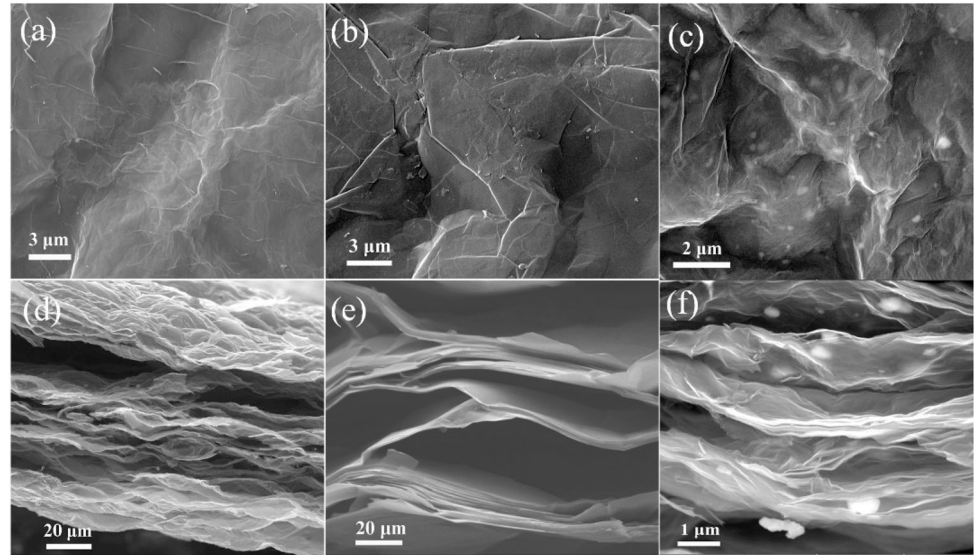


Fig. 3 **a** High-resolution TEM image of Fe₃O₄@GF. **b** Close view of lattice fringe of Fe₃O₄ nanoparticles

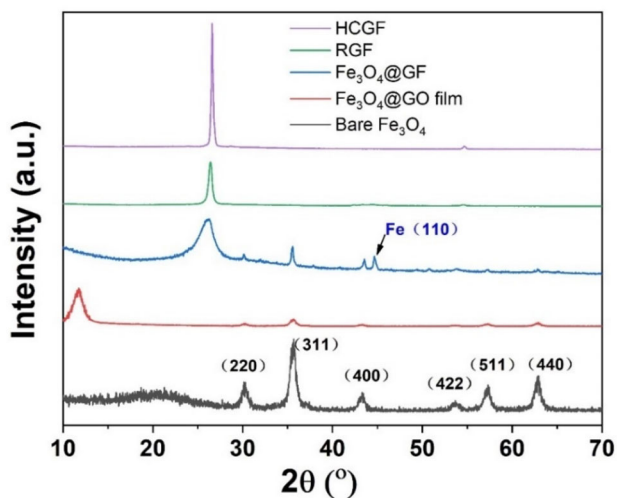
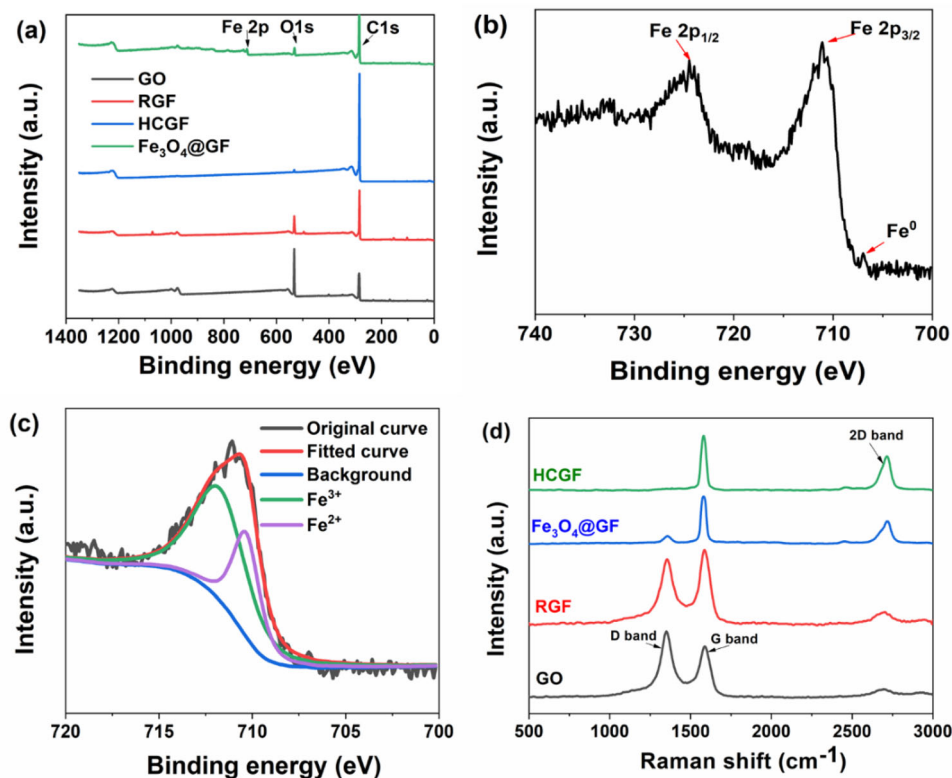


Fig. 4 XRD pattern of bare Fe₃O₄, Fe₃O₄@GO film, Fe₃O₄@GF, RGF and HCGF

26.1°, owing to the removal of oxygen-containing functional groups. The diffraction peaks of Fe₃O₄ become sharper and stronger compared with Fe₃O₄@GO film, indicating that the grain size and crystallinity of Fe₃O₄ are increased after thermal treatment. Moreover, a new diffraction peak appears at 2θ = 44.7°, which could be corresponding to the (110) plane of iron [32]. The generation of the iron is related to the catalytic graphitization reaction. Based on previous reports, the catalytic graphitization due to Fe₃O₄ might be explained by the formation of carbide (Fe₃C); then, Fe₃C was decomposed into iron and graphitic carbon [25–27], which was why the prepared Fe₃O₄@GF contains iron. The resulting iron could also act as a catalyst for graphitization of GO. Under the synergy of Fe₃O₄ and iron, the highly ordered graphitic structure was obtained at a low calcination temperature.

The elemental composition and chemical state of the samples were further investigated via XPS testing. The C 1s and O 1s peaks can be observed in the XPS spectra of all tested samples (Fig. 5a); in contrast, the Fe 2p peak only appears in the XPS spectrum of Fe₃O₄@GF. For the GO film, the intensity of the O 1s peak is considerably higher than that of the C1s peak because of the abundant oxygen-containing functional groups on the GO film. The removal of oxygen-containing functional groups during graphitization significantly decreases the intensity of the O 1s peak.

Fig. 5 **a** XPS survey spectra of GO, RGF, HCGF and Fe₃O₄@GF. **b** XPS spectrum of Fe 2p peak of Fe₃O₄@GF. **c** XPS spectrum of fitted Fe 2p peak of Fe₃O₄@GF. **d** Raman spectra of GO, RGF, HCGF and Fe₃O₄@GF



Moreover, the O 1s peak of Fe₃O₄@GF is less intense than that of RGF, which implies that introducing Fe₃O₄ may facilitate the removal of oxygen-containing functional groups on the GO surface. This conclusion is also supported by the fitted C 1s peak (Fig. S2).

The C 1s spectra of all samples are composed of two components, which are ascribed to the C–C (~ 284.8 eV) and C–O (~ 286.4 eV) groups [33, 34]. The intensity of the peaks corresponding to the C–O groups clearly decreases after thermal reduction, which is consistent with the results of XPS survey spectra. The area ratio of the deconvoluted C–C peak to C–O peak can be calculated as 3.33:1 for Fe₃O₄@GF, 2.55:1 for RGF, and 3.51:1 for HCGF, which indicates that Fe₃O₄@GF can be reduced more easily than RGF.

Figure 5b shows the Fe 2p XPS spectrum of Fe₃O₄@GF, wherein two peaks appear at 724.5 and 711.1 eV, corresponding to the Fe 2p_{1/2} and Fe 2p_{3/2} orbitals of Fe₃O₄ [30, 33], respectively. The weak satellite peak at 707.0 eV is induced by Fe⁰ [32], indicating the presence of iron in Fe₃O₄@GF. The Fe 2p_{3/2} peak can be deconvoluted into two peaks at 711.7 and 710.4 eV (Fig. 5c), which are ascribed to

Fe³⁺ and Fe²⁺ of Fe₃O₄ [26, 30], respectively. The area ratio between the deconvoluted Fe³⁺ peak and the Fe²⁺ peak is calculated as 2.09:1, which matches well with the atomic ratio of Fe³⁺/Fe²⁺ in Fe₃O₄. Finally, we investigated the O 1s XPS spectra of the samples. Unlike the single peaks of GO, RGF, and HCGF, the O 1s XPS spectrum of Fe₃O₄@GF exhibits distinct double peaks due to C–O and Fe–O bonds (Fig. S3).

Raman spectroscopy was conducted to estimate and compare the graphitization degree of the samples. Figure 5d reveals two characteristic peaks at 1352 cm⁻¹ (D band) and 1579 cm⁻¹ (G band), which are induced by lattice defects and the tangential stretching mode of sp²-hybridized carbon atoms [35, 36], respectively. The I_D/I_G ratio can be used to evaluate the graphitization degree of carbon-containing materials. Compared with GO, the I_D/I_G ratio of Fe₃O₄@GF significantly decreases from 1.29 to 0.06, suggesting that numerous defects are repaired during calcination process. Moreover, the D band of Fe₃O₄@GF is much less intense than that of RGF, which indicates that Fe₃O₄@GF can obtain higher graphitization degree than the bare graphene film at the same annealing temperature. This phenomenon can be attributed to the catalytic graphitization effect

of Fe₃O₄ and Fe. The D band of HCGF almost disappears, indicating its higher graphitization degree than Fe₃O₄@GF. This can be attributed to the ultra-high graphitization temperature of HCGF, which enable more structural defects to be repaired. Furthermore, 2D bands located at $\sim 2715\text{ cm}^{-1}$ show an increasing trend from GO, RGF, Fe₃O₄@GF to HCGF, which also demonstrates that the structure of Fe₃O₄@GF is more ordered than RGF, but more disordered than HCGF.

3.4 Thermal and electrical properties of Fe₃O₄@GF

The thermal and electrical conductivity of carbon materials significantly increases after graphitization owing to deoxygenation, structure rearrangement, and defect repair [15, 16]. Herein, we compare the thermal and electrical properties of Fe₃O₄@GF, RGF, and HCGF with similar thicknesses of $\sim 50\ \mu\text{m}$ to further verify the catalytic graphitization effect of Fe₃O₄. As presented in Fig. 6, the thermal conductivity of Fe₃O₄@GF ($973\text{ W m}^{-1}\text{ K}^{-1}$) is substantially higher than that of RGF ($729\text{ W m}^{-1}\text{ K}^{-1}$), indicating that catalytic graphitization assisted by Fe₃O₄ repairs more defects than graphitization without catalyst. The thermal conductivity of Fe₃O₄@GF is no match for that of HCGF ($1278\text{ W m}^{-1}\text{ K}^{-1}$), owing to its more disordered structure than HCGF and the increasing phonon scattering at the interfaces between graphene sheets and Fe₃O₄ nanoparticle. The measured electrical conductivity mirrors the thermal conductivity (Fig. 6), further confirming catalytic graphitization by Fe₃O₄ and Fe.

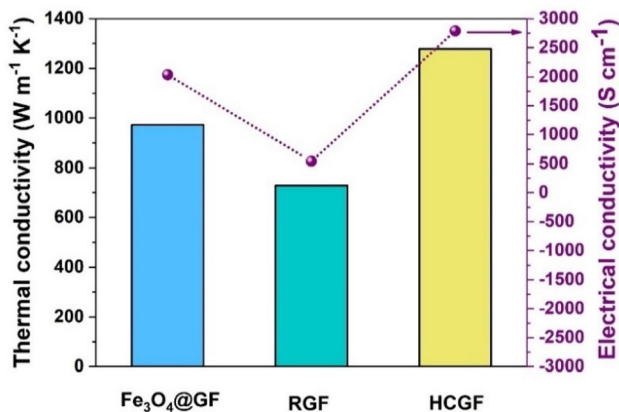


Fig. 6 Thermal and electrical conductivity of RGF, HCGF, and Fe₃O₄@GF

3.5 EMI shielding performance of Fe₃O₄@GF

It is well known that the EMI shielding performance is associated with the electromagnetic parameters. Therefore, the relative permittivity and permeability of the samples were investigated in the X-band (8.2–12.4 GHz) based on the coaxial transmission line method. As shown in Fig. 7a, the mean relative permittivity of Fe₃O₄@GF, RGF, and HCGF is 7.56, 6.62, and 7.48, respectively. The enhanced relative permittivity of Fe₃O₄@GF is attributed to strong interfacial polarization caused by the introduction of Fe₃O₄ nanoparticles. Figure 7b displays the relative permeability of all samples. The mean relative permeability of RGF and HCGF is close to 1, owing to their nonmagnetic properties. In contrast, the mean relative permeability of Fe₃O₄@GF is increased to 1.51 due to the introduction of magnetic Fe₃O₄ nanoparticles. The increased permeability causes a remarkable decrease of skin depth δ according to Eq. (2) [37, 38],

$$\delta = (\pi\sigma f\mu)^{-\frac{1}{2}} \quad (2)$$

Here, σ represents the electrical conductivity of the material, and f is the frequency of the electromagnetic wave. The skin depth is defined as penetrating distance of electromagnetic wave in materials at which electromagnetic energy is attenuated to $1/e$ of the initial value. A small skin depth means a good shielding performance of the material.

The EMI SE of Fe₃O₄@GF was investigated, which is widely used in radar detection, weather monitoring, and satellite communication. The EMI measurement setup is displayed in Fig. 7c. The EMI SE was measured experimentally via commonly used vector network analyzer equipped with waveguide section. Because the thickness affects the EMI SE of materials, we used samples of similar thicknesses ($\sim 50\ \mu\text{m}$) for the measurements. Figure 7d shows that the average SE of HCGF ($\sim 46.20\text{ dB}$) is higher than that of RGF ($\sim 33.45\text{ dB}$), which is attributed to the superior electrical conductivity of the former. Moreover, Fe₃O₄@GF has an average EMI SE of 52.76 dB , which is higher than that of HCGF and RGF due to the contribution of Fe₃O₄ nanoparticles. For comparison, the EMI SE and thickness of recently reported carbon-based EMI shielding materials [6, 15, 17, 33, 39–42] in the X-band are presented in

Fig. 7 **a** Relative permittivity and **b** relative permeability of RGF, HCGF, and Fe₃O₄@GF in the X-band; **c** photograph of EMI shielding measurement setup based on waveguide method; **d** EMI SE of RGF, HCGF, and Fe₃O₄@GF in the X-band; **e** EMI shielding performance of recently reported graphene-based materials; **f** schematic representation of EMI shielding mechanism of Fe₃O₄@GF

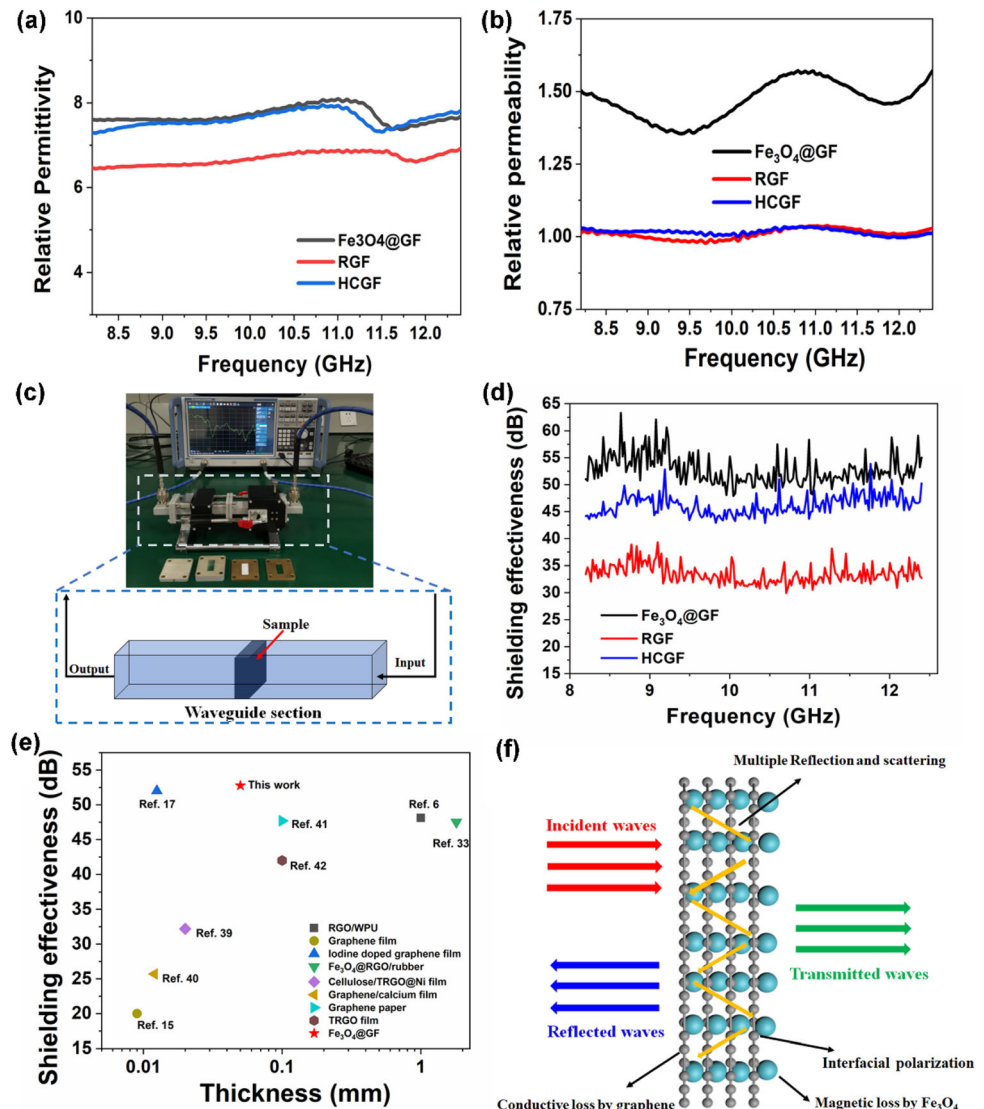


Fig. 7e. The EMI SE of Fe₃O₄@GF is superior to most of relevant shielding materials ever reported. Moreover, the thinner thickness makes our prepared materials have wider applications in portable electronic devices.

As well known, the electromagnetic waves can be shielded by a material through reflection mechanism and absorption mechanism. The total EMI SE is the sum of attenuation from reflection (SE_R) and absorption (SE_A). As shown in Fig. 7f, the SE_R depends on the impedance mismatch between the film and free space (air) in which the incident electromagnetic wave travels. SE_A represents the ability of the film to convert electromagnetic energy into thermal energy [43], including conductive loss caused by graphene, magnetic loss caused by Fe₃O₄,

interfacial polarization as well as multiple reflection and scattering.

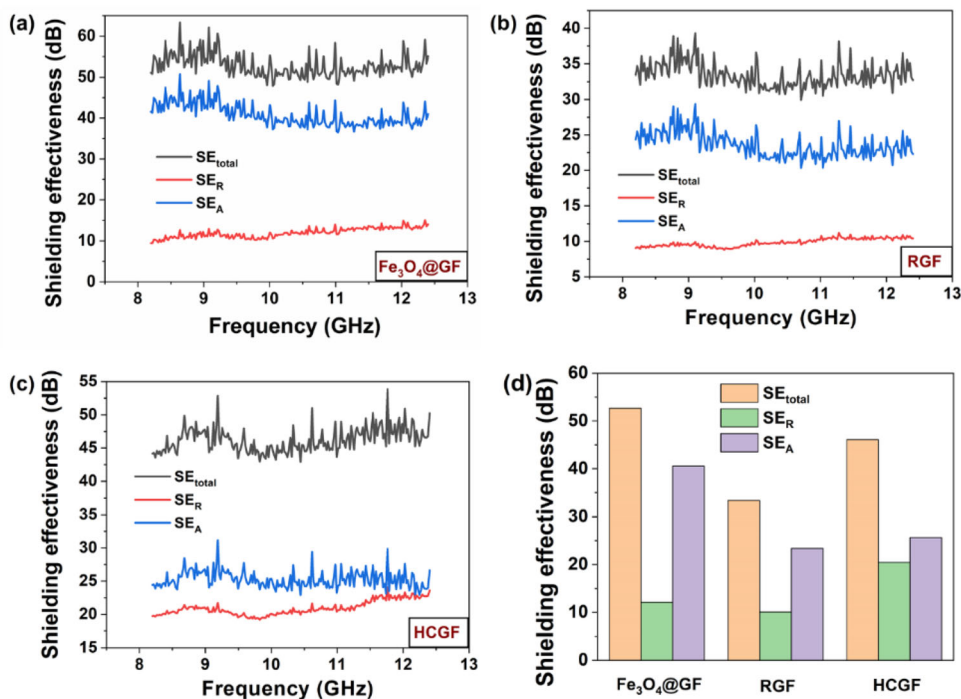
To explore the shielding mechanism of Fe₃O₄@GF, we calculate SE_R and SE_A from the scattering parameters using Eqs. (3) and (4) [44, 45],

$$SE_R = -10 \log(1 - R) = -10 \log(1 - S_{11}^2) \quad (3)$$

$$SE_A = -10 \log\left(\frac{T}{1 - R}\right) = -10 \log\left(\frac{S_{21}^2}{1 - S_{11}^2}\right) \quad (4)$$

where T and R are the transmittance and reflectivity of the electromagnetic waves, respectively. The scattering parameters (S_{11} and S_{21}) were measured using the vector network analyzer. Figure 8a shows that both reflection and absorption contribute to the EMI SE of Fe₃O₄@GF. The mean value of SE_A

Fig. 8 SE_{total} , SE_R , and SE_A of **a** RGF, **b** HCGF, and **c** $Fe_3O_4@GF$ in the X-band. **d** The comparison of average SE_{total} , SE_R , and SE_A of RGF, HCGF, and $Fe_3O_4@GF$



(~ 40.68 dB) is much higher than that of SE_R (~ 12.08 dB), indicating that absorption is the dominant shielding mechanism for $Fe_3O_4@GF$. Furthermore, the high conductivity of HCGF deteriorates the impedance match between the air and the film, resulting in a higher SE_R value than that of RGF and $Fe_3O_4@GF$ (Fig. 8d). Moreover, SE_A of $Fe_3O_4@GF$ is higher than that of the bare graphene film, which means that $Fe_3O_4@GF$ can absorb more electromagnetic energy than the other samples. The enhanced SE_A of $Fe_3O_4@GF$ results from the contribution of Fe_3O_4 nanoparticles. On the one hand, Fe_3O_4 nanoparticles can attenuate electromagnetic waves through magnetic loss, such as natural resonance and eddy-current loss [46, 47]. On the other hand, charges are prone to accumulate at the interface between graphene and Fe_3O_4 under an alternating electromagnetic field, resulting in interfacial polarization and dielectric loss [48–50].

4 Conclusion

In summary, Fe_3O_4 nanoparticles anchored graphene films were successfully prepared via in situ wet chemical synthesis followed by catalytic graphitization at a moderate annealing temperature of 1000 °C. The magnetic film exhibits a high thermal

conductivity of $973 \text{ W m}^{-1} \text{ K}^{-1}$ and an electrical conductivity of $\sim 2.0 \times 10^3 \text{ S cm}^{-1}$. The EMI SE of $Fe_3O_4@GF$ can reach as high as 52.76 dB in the X-band at a thickness of $\sim 50 \mu\text{m}$, which is superior to most of carbon-based shielding materials. The good EMI shielding performance is attributed to the introduction of Fe_3O_4 nanoparticles and high graphitization degree of graphene sheets. With these excellent properties, $Fe_3O_4@GF$ is expected to be a promising candidate for EMI shielding application in portable electronic devices, such as mobile phones and notebook computers.

Acknowledgements

This work was supported by the Youth Science Foundation of Shanxi Province (201901D211576 and 202103021223453) and General Projects of Natural Science Research of Shanxi Province (202103021224448).

Author contributions

WL did methodology, investigation, formal analysis, data curation, writing—original draft, and funding acquisition. KJ was involved om validation, formal

analysis, and funding acquisition. DW performed formal analysis, writing—review and editing. XW contributed to conceptualization, methodology, writing—review & editing. PW done writing—review and editing. KZ performed resources and writing—review and editing.

Funding

Youth Science Foundation of Shanxi Province, 201901D211576, Wei Liu, 202103021223453, Kun Jia, General Projects of Natural Science Research of Shanxi Province, 202103021224448, Wei Liu.

Data availability

All data generated or analyzed during the current study are available from the corresponding author on reasonable request.

Declarations

Conflict of interest The authors declare that they have no conflict of interest.

Supplementary Information: The online version contains supplementary material available at <http://doi.org/10.1007/s10854-022-09136-2>.

References

1. Y. Bhattacharjee, I. Arief, S. Bose, *J. Mater. Chem. C* **5**, 7390–7403 (2017)
2. A.K. Singh, A. Shishkin, T. Koppel, N. Gupta, *Compos. Part B*. **149**, 188–197 (2018)
3. C. Wang, V. Murugadoss, J. Kong, Z. He, X. Mai, Q. Shao, Y. Chen, L. Guo, C. Liu, S. Angaiah, Z. Guo, *Carbon* **140**, 696–733 (2018)
4. J. Yin, J. Zhang, S. Zhang, C. Liu, X. Yu, L. Chen, Y. Song, S. Han, M. Xi, C. Zhang, N. Li, Z. Wang, *Chem. Eng. J.* **421**, 129763 (2021)
5. S. Sankaran, K. Deshmukh, M.B. Ahamed, S.K.K. Pasha, *Compos. Part A*. **114**, 49–71 (2018)
6. Y. Wang, W. Wang, R. Xu, M. Zhu, D. Yu, *Chem. Eng. J.* **360**, 817–828 (2019)
7. Q.W. Wei, S.F. Pei, X.T. Qian, H.P. Liu, Z.B. Liu, W.M. Zhang, T.Y. Zhou, Z.C. Zhang, X.F. Zhang, H.M. Cheng, W.C. Ren, *Adv. Mater.* **32**, 1907411 (2020)
8. Y.J. Wan, P.L. Zhu, S.H. Yu, R. Sun, C.P. Wong, W.H. Liao, *Small* **14**, 1800534 (2018)
9. X. Fan, G. Zhang, J. Li, Z. Shang, H. Zhang, Q. Gao, J. Qin, X. Shi, *Compos. Part A*. **121**, 64–73 (2019)
10. Y. Zhan, M. Oliviero, J. Wang, A. Sorrentino, G.G. Buonocore, L. Sorrentino, M. Lavorgna, H. Xia, S. Iannace, *Nanoscale* **11**, 1011–1020 (2019)
11. B. Shen, Y. Li, W. Zhai, W. Zheng, *A.C.S. Appl. Mater. Interfaces*. **8**, 8050–8057 (2016)
12. Y.Y. Wang, W.J. Sun, D.X. Yan, K. Dai, Z.M. Li, *Carbon* **176**, 118–125 (2021)
13. A.A. Khodiri, M.Y. Al-Ashry, A.G. El-Shamy, *J. Alloys. Compd.* **847**, 156430 (2020)
14. S. Ganguly, S. Ghosh, P. Das, T.K. Das, S.K. Ghosh, N.C. Das, *Polym. Bull.* **77**, 2923–2943 (2020)
15. B. Shen, W. Zhai, W. Zheng, *Adv. Func. Mater.* **24**, 4542–4548 (2014)
16. S. Lin, S. Ju, J. Zhang, G. Shi, Y. He, D. Jiang, *RSC Adv.* **9**, 1419–1427 (2019)
17. Y.J. Wan, P.L. Zhu, S.H. Yu, R. Sun, C.P. Wong, W.H. Liao, *Carbon* **122**, 74–81 (2017)
18. M.S. Cao, X.X. Wang, W.Q. Cao, J. Yuan, *J. Mater. Chem. C*. **3**, 6589–6599 (2015)
19. S. Lin, S. Ju, G. Shi, J. Zhang, Y. He, D. Jiang, *J. Mater. Sci.* **54**, 7165–7179 (2019)
20. Z. Wang, B. Mao, Q. Wang, J. Yu, J. Dai, R. Song, Z. Pu, D. He, Z. Wu, S. Mu, *Small* **14**, 1704332 (2018)
21. H.J. Chen, J.X. Yang, Q. Shuai, J. Li, Q. Ouyang, S. Zhang, *Compos. Sci. Technol.* **200**, 108455 (2020)
22. Y. Liu, Q. Liu, J. Gu, D. Kang, F. Zhou, W. Zhang, Y. Wu, D. Zhang, *Carbon* **64**, 132–140 (2013)
23. H.B. Ouyang, Q.Q. Gong, C.Y. Li, J.F. Huang, Z.W. Xu, *Mater. Lett.* **235**, 111–115 (2019)
24. M. Bayat, H. Yang, F. Ko, *Polymer*. **52**, 1645–1653 (2011)
25. T. Zhang, D. Huang, Y. Yang, F. Kang, J. Gu, *Polymer* **53**, 6000–6007 (2012)
26. B. Mordina, R. Kumar, R.K. Tiwari, D.K. Setua, A. Sharma, *J. Phys. Chem. C*. **121**, 7810–7820 (2017)
27. T. Zhang, D.Q. Huang, Y. Yang, F.Y. Kang, J.L. Gu, *Mater. Sci. Eng. B* **178**, 1–9 (2013)
28. J. Liang, Y. Xu, D. Sui, L. Zhang, Y. Huang, Y. Ma, F. Li, Y. Chen, *J. Phys. Chem. C*. **114**, 17465–17471 (2010)
29. Y. Liu, Y. Zhan, Y. Ying, X. Peng, *New. J. Chem.* **40**, 2649–2654 (2016)
30. S. Majumder, M. Sardar, B. Satpati, S. Kumar, S. Banerjee, *J. Phys. Chem. C*. **122**, 21356–21365 (2018)
31. A.A. Khodiri, M.Y. Al-Ashry, A.G. El-Shamy, *J. Alloy. Compd.* **847**, 156430 (2020)
32. J. Sun, P. Zan, X. Yang, L. Ye, L. Zhao, *Electrochim. Acta*. **215**, 483–491 (2016)

33. Y. Zhan, J. Wang, K. Zhang, Y. Li, Y. Meng, N. Yan, W. Wei, F. Peng, H. Xia, *Chem. Eng. J.* **344**, 184–193 (2018)
34. X.H. Li, X. Li, K.N. Liao, P. Min, T. Liu, A. Dasari, Z.Z. Yu, *A.C.S. Appl. Mater. Interfaces.* **8**, 33230–33239 (2016)
35. X. Yin, H. Li, L. Han, J. Meng, J. Lu, L. Zhang, W. Li, Q. Fu, K. Li, Q. Song, *Chem. Eng. J.* **387**, 124025 (2020)
36. T. Kuang, L. Chang, F. Chen, Y. Sheng, D. Fu, X. Peng, *Carbon* **105**, 305–313 (2016)
37. H.Y. Choi, T.W. Lee, S.E. Lee, J. Lim, Y.G. Jeong, *Compos. Sci. Technol.* **150**, 45–53 (2017)
38. J. Xi, Y. Li, E. Zhou, Y. Liu, W. Gao, Y. Guo, J. Ying, Z. Chen, G. Chen, C. Gao, *Carbon* **135**, 44–51 (2018)
39. G. Han, Z. Ma, B. Zhou, C. He, B. Wang, Y. Feng, J. Ma, L. Sun, C. Liu, *J. Colloid Interf. Sci.* **583**, 571–578 (2021)
40. L.C. Jia, W.J. Sun, C.G. Zhou, D.X. Yan, Q.C. Zhang, Z.M. Li, *J. Mater. Chem. C.* **6**, 9166–9174 (2018)
41. W.L. Song, L.Z. Fan, M.S. Cao, M.M. Lu, C.Y. Wang, J. Wang, T.T. Chen, Y. Li, Z.L. Hou, J. Liu, Y.P. Sun, *J. Mater. Chem. C.* **2**, 5057–5064 (2014)
42. L.J. Xu, W.Q. Zhang, L.D. Wang, J. Xue, S.F. Hou, *RSC Adv.* **11**, 33302–33308 (2021)
43. J. Kang, D. Kim, Y. Kim, J.B. Choi, B.H. Hong, S.W. Kim, *2D Mater.* **4**, 025003 (2017)
44. W. Liu, T. Yao, K. Jia, J. Gu, D. Wang, X. Wei, *J. Mater. Sci. Mater. Electron.* **32**, 4393–4403 (2021)
45. S. Zeng, X. Li, M. Li, J. Zheng, E. Shiju, W. Yang, B. Zhao, X. Guo, R. Zhang, *Carbon* **155**, 34–43 (2019)
46. X.T. Yang, S.G. Fan, Y. Li, Y.Q. Guo, Y.G. Li, K.P. Ruan, S.M. Zhang, J.L. Zhang, J. Kong, J.W. Gu, *Compos. Part A.* **128**, 105670 (2020)
47. W.L. Song, X.T. Guan, L.Z. Fan, W.Q. Cao, C.Y. Wang, Q.L. Zhao, M.S. Cao, *J. Mater. Chem. A.* **3**, 2097–2107 (2015)
48. L. Wang, H. Qiu, C. Liang, P. Song, Y. Han, Y. Han, J. Gu, J. Kong, D. Pan, Z. Guo, *Carbon* **141**, 506–514 (2019)
49. A.P. Singh, M. Mishra, P. Sambyal, B.K. Gupta, B.P. Singh, A. Chandra, S.K. Dhawan, *J. Mater. Chem. A.* **2**, 3581–3593 (2014)
50. A.V. Menon, B. Choudhury, G. Madras, S. Bose, *Chem. Eng. J.* **382**, 122816 (2020)

Publisher's Note Springer Nature remains neutral with regard to jurisdictional claims in published maps and institutional affiliations.

Springer Nature or its licensor holds exclusive rights to this article under a publishing agreement with the author(s) or other rightsholder(s); author self-archiving of the accepted manuscript version of this article is solely governed by the terms of such publishing agreement and applicable law.